Construction and Building Materials 326 (2022) 126640

Contents lists available at ScienceDirect

Construction and Building Materials

journal homepage: www.elsevier.com/locate/conbuildmat

Experimental characterization of the textile-to-mortar bond through distributed optical sensors

Elisa Bertolesi [a,*], Mario Fagone [b], Tommaso Rotunno [c], Ernesto Grande [d], Gabriele Milani [e]

[a] Department of Civil and Environmental Engineering, Brunel University London, Uxbridge UB8 3PH, United Kingdom
[b] Department of Civil and Environmental Engineering, University of Florence, via di S. Marta 3, Florence 50139, Italy
[c] Department of Architecture, University of Florence, Piazza Brunelleschi 6, Florence 50121, Italy
[d] Department of Engineering Science, University Guglielmo Marconi, Via Plinio 44, Rome 00193, Italy
[e] Department of Architecture, Built Environment and Construction Engineering (ABC), Politecnico di Milano, Piazza Leonardo da Vinci 32, Milan 20133, Italy

ARTICLE INFO

Keywords:
Fiber optic sensors
Debonding mechanisms
TRM & FRCM composite materials
Bond-slip model
Strengthening

ABSTRACT

TRM (Textile Reinforced Mortar) and FRCM (Fiber Reinforced Cementitious Mortar) strengthening materials are highly heterogeneous composites involving domains that have dramatically different mechanical properties (i.e., inorganic matrix and fabric textile). Maximizing their exploitation ratio involves achieving a better bond between textile and inorganic matrix which shifts the failure mode from textile sliding to textile rupture or cohesive failure modes. So far, the local bond behaviour between fiber bundles and inorganic matrix has been analysed indirectly through the evaluation of the global performance of TRM/FRCM materials subjected to tensile tests or single lap shear tests. In this article, the authors adopted distributed fiber optic sensors directly installed to textile bundles to track the strain evolutions of PBO-TRM strengthening materials. The strain evolutions were used, for the first time, (i) to understand the behaviour of TRM coupons subjected to tensile tests and (ii) to experimentally calibrate the interfacial tangential bond-slip law in flat masonry pillars strengthened with TRMs. The results allowed a better insight of the response of TRM materials not possible with traditional sensors and an accurate characterization of their bond performance. The interfacial tangential stress-slip law was then adopted in analytical models to predict the global performance of TRM materials providing satisfactory results compared with experimental outcomes.

1. Introduction

Cohesive material laws describe the complex detachment mechanism of strengthening materials from brittle supports with simplified mathematical relationships [1–4]. From an operational point of view, this simplification represents a convenient solution to accurately study detachment phenomena that otherwise would involve highly nonlinear computational approaches and damage material models [5–8]. The reliability of the proposed bond-slip laws, which evolved over the years from piecewise linear to linear and exponentially decreasing softening laws, is usually assessed through experimental investigations. The technical literature is abundant in terms of experimental research works confirming different mathematical descriptions of the bond performance of Fiber Reinforced Polymer (FRP) composites applied on brittle supports [1–4]. Indeed, detachment of FRPs from concrete or masonry supports involves, depending on the support quality, cohesive failures of the support itself. Thus, most of the observed damages is localized in an interfacial layer, whereas composites and supports generally behave as elastic materials. When it comes to composite strengthening materials involving constituent materials that have dramatically different mechanical and physical properties such as TRMs (Textile Reinforced Mortar) and FRCMs (Fiber Reinforced Cementitious Mortar), the assessment of their bond quality became an intricated problem [9–15]. Giving the high heterogeneity of their constituent materials (i.e., inorganic matrix and fiber textiles) in terms of elastic and inelastic properties, the observed failure modes comprise a wide range of possibilities [16], including: (i) cohesive debonding in the masonry; (ii) debonding at the matrix-to-substrate; (iii) debonding at the textile-to-matrix interface; (iv) sliding of the textile within the matrix; and (v) tensile rupture of the textile. According to the technical literature, failure modes involving sliding of the textile and matrix-to-textile detachment are associated with a poor bond and thus to a lower exploitation ratio of the strengthening materials itself. Improving the bond between the constituent materials, especially textile and mortar matrix, ensures higher

* Corresponding author.

https://doi.org/10.1016/j.conbuildmat.2022.126640
Received 5 November 2021; Received in revised form 14 January 2022; Accepted 26 January 2022
Available online 17 February 2022

Table 1
Bricks mechanical properties; C.V. = coefficient of variation.

	n. specimens	Mean	C.V.
		[MPa]	[%]
Compressive strength	18	20.10	10.79
Young modulus	6	8712	6.92
Direct tensile strength	6	2.49	16.90
Bending tensile strength	6	3.36	33.77

Table 2
Three point bending tensile strength and compressive strength of mortar.

	n. specimens	Mean	C.V.
		[MPa]	[%]
(Bending) tensile strength	6	1.85	9.42
Compressive strength	12	5.18	8.212

exploitation ratios of the strengthening intervention. This is usually associated with failure modes (i) and (v). Results from [17] clearly indicate that the bond capacity is not directly related to the textile tensile strength or stiffness but depends on the interaction between textile and matrix as well as to that between composite system and substrate. Thus, understanding the bond quality between textile and mortar matrix is of paramount importance to: (i) improve exploitation ratios of TRM and FRCM strengthening materials, (ii) calibrate mathematical interfacial bond-slip laws [18–24] and (iii) provide reliable guidelines for their design [16,25–27]. From an experimental point of view, the study of the local bond between textiles and inorganic matrices in TRM or FRCM materials was performed conducting tensile tests on coupons [28–29] and single/double lap shear tests [30–31]. Unfortunately, the corpus of the experimental investigations done so far, failed in providing accurate data on the matrix-fibre interaction, thus suggesting further investigation is still needed. The available experimental data refer to TRM/FRCM macroscopic behaviour (i.e., failure modes, force-slip curves, maximum elongation and peak loads) leaving several open issues still unresolved. Tensile tests are used to provide the constitutive relationship of TRM/FRCM composites, which is generally characterized by three response stages, whereas single/double lap shear tests are preferred to estimate the bond capacity transferred from the structural element to the externally bonded strengthening. In [17], de Felice et al. clearly identify that the weakest element controlling the bond capacity change from system to system, depending on multiple aspects, which cannot be directly inferred from tensile tests. Several attempts were done to investigate the bond quality between textiles and inorganic matrices through pull-out tests of single bundles from matrix cubic specimens [32–33]. Although those investigations provided valuable insights of the local bond, the scale change between single bundle bond and textile bond add a further level of complexity to the problem and the actual assessment of what happens locally during detachment phenomena is still one of the most important and, so far unresolved, issues for TRM/FRCM materials. This is mostly due to the fact that traditional sensors are only able to provide global measurements which are suitable for FRPs reinforced structures but not for TRM/FRCM strengthening materials. Recently, many civil engineering fields are seeing the introduction of new sensing technologies such as wavelength- or frequency-based fiber optic sensors [34–37]. Fiber optic sensors are based on interrogation of strain-induced wavelength shifts. Introduction of Bragg gratings in optical fibers usually is performed exposing optical fiber core to intense UV laser through a mask to achieve specific wavelength reflectivity. Conversely to traditional sensors (i.e., LVDTs DIC and strain gauges), such sensors provide several advantages, namely: (i) high sensitivity, (ii) ease of installation, (iii) capability of static and dynamic measurements. In addition, they can be serially multiplexed by writing several Bragg gratings of different wavelengths on one length of optical fiber and be embedded into different materials (i.e., asphalt, concrete, etc). The present paper is intended to provide, for the first time, the local interfacial tangential-bond slip law obtained experimentally through Fibre Optic (FO) sensors embedded into TRM/FRCM materials. The article is organized into five sections, including a comprehensive description of the experimental investigation comprising tensile and single laps shear tests of PBO (polyparaphenylene benzobisoxazole) FRCM strengthening materials applied to flat masonry pillars (Section 2) and the adopted Fiber Optic technology. Sections 3 discusses the calibration procedure used to obtain the interfacial bond-slip law fed with the strain evolutions tracked using fiber optic sensors. Finally, Section 4 critically discusses the outcomes obtained using an analytical model developed by the authors and herein coupled with the interfacial bond law obtained from the present experimental investigation. Final remarks and future works are highlighted in Section 5.

2. Experimental investigation

The experimental investigation concerned a FRCM coupon subjected to tensile test according to [38] and a masonry pillar strengthened with FRCM materials subjected to a single lap shear test according to [16]. The masonry pillar was manufactured using bricks and mortar having the same characteristics of the ones utilized by the authors in previous experimental campaigns. Therefore, only the main mechanical properties of such materials are reported in the following since the mechanical characterization of mortar and bricks has already been fully described in [39–40]. For further details, the reader can refer to the cited papers. The FRCM strengthening system considered in this paper is composed of an inorganic matrix and a bi-directional PBO fiber mesh (70 g/m^2 in warp and 18 g/m^2 in weft). The main mechanical characteristics of the materials composing the FRCM system, declared by the supplier in the technical data sheet, are reported in the following.

2.1. Materials properties

2.1.1. Bricks and mortar

Solid pressed bricks, also called soft mud firebricks, and ready mixed mortar made with lime and cement as binder were used in manufacturing the masonry pillar. Those materials were considered because their characteristics are similar to those of the materials commonly present in most of the existing masonry constructions in Italy. The mechanical characterization of the bricks was carried out by subjecting 18 cubic specimens (50×50×50 mm^3) and six prismatic specimens (50×50×150 mm^3) to compression tests, 6 prismatic specimens (40×40×200 mm^3) to three-point bending tests and, finally, 6 prismatic specimens (40×40×90 mm^3) to direct tensile tests. The test results are summarized in Table 1.

For the characterization of the mechanical parameters of the mortar, six 40×40×160 mm^3 specimens were subjected to three-point bending tests. Then, compression tests were performed on the twelve halves of the prisms. The tests were performed according to [41]. The average strength values are shown in Table 2 as well as the coefficient of variation.

2.1.2. Fiber reinforced cementitious matrix (FRCM)

Bi-directional PBO mesh and stabilized inorganic matrix (a cement-based mortar with short fibers) are the components of the strengthening system used in the present experimental investigation. The mechanical properties declared by the supplier in the technical data sheet are summarized in Table 3.

2.2. Distributed fiber optic sensors

This study adopted distributed fiber optic (FO) strain sensors to measure the local interfacial bond law in FRCM/TRM strengthening materials. The FO technology employed in the present study is based on

Table 3
Mechanical properties (declared by the producer) of the reinforcing system components.

	Equivalent thickness of the mesh (warp direction)	Tensile Young's modulus (E_f) of the fibre/mesh	Ultimate elongation of the fibre.	Toughness	Compressive strength at 28 days	Compressive Young's modulus at 28 days	Bending strength at 28 days
	[mm]	[GPa]	[%]	[GPa]	[MPa]	[MPa]	[MPa]
PBO fibre	–	270	2.5	5.80	–	–	–
Bi-directional PBO mesh	0.045	241	–	–	–	–	–
Inorganic matrix	–	–	–	–	≥ 20	≥ 7500	≥ 3.5

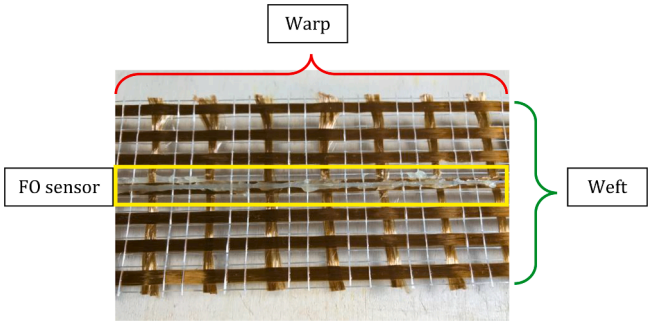

Fig. 1. Distributed fiber optic sensor adopted in the present investigation.

classical Rayleigh scattering. The irregularities allowing the elastic scattering of the transmitted light inside the glass core, are generated during the FO manufacturing, and they are directly linked to the wavelengths of the light wave.

The FO sensor comprises a coated fibre having 125 μm cladding diameter, a GFRP outer diameter of 0.5 mm and an additional High-Density Polyethylene (HDPE) outer jacket (diameter 0,2 mm). The coating layer was designed to protect the inner fiber during the installation and testing operations. This study used a dynamic data acquisition system to perform the measurement. The frequency shift is associated with strain changes, as described in Eq. (1):

$$\varepsilon = \frac{1}{k}\ln\frac{\lambda}{\lambda_0} \tag{1}$$

At a constant temperature, the spectral shift can be converted into strain along the FO distributed sensor with a calibrated strain sensitivity coefficient (k). Actual (λ) and reference (λ_0) wavelengths are automatically calculated by the FO dynamic interrogator. The distributed FO sensor comprises 6 measuring points with 8 mm grating length and 26 mm geometrical spacing reaching a total sensing length equal to 130 mm (spacing between first and last mid-section of the FOs). Two different acquisition frequencies were used, namely 100 and 50 Hz for the tensile (the FO sensor is schematically depicted in Fig. 3a) and the single lap shear (the FO sensor is schematically depicted in Fig. 7a) tests, respectively. No temperature compensation was considered in the present study. Fig. 1

2.3. Tensile test

Tensile test on the coupon specimen was carried out according to [38]. The specimen, composed of two layers of mortar and a single layer of PBO fiber mesh, had total thickness of 8 mm and length 500 mm; a textile fabric portion composed of seven yarns in the warp direction was considered, so that the coupon had width equal to 63 mm (see Fig. 2a). Before manufacturing the specimen, a FO sensor was installed to the central part of the fabric in the warp direction (see Fig. 2b). According to the indications provided by the supplier, the specimen was manufactured through a wet-lay-up procedure (see Fig. 2c): a first layer of matrix was laid in a wood framework having thickness of 4 mm; then, a single layer of PBO mesh was positioned on it taking care that this adheres to the matrix by exerting a slight pressure; a second wood framework (4 mm thick) was positioned on the first one so that the second layer of matrix could be applied. The specimen was cured at room conditions for at least 28 days before testing.

According to [38] the upper and lower parts of the specimen, having a length of 125 mm (Fig. 2a), were clamped using stiff steel plates with a rubber sheet in between (Fig. 3). Such plates were tightened using a

Fig. 2. Coupon specimen geometry (-a), FO sensor glued to the PBO mesh (-b) and coupon manufacturing (-c).

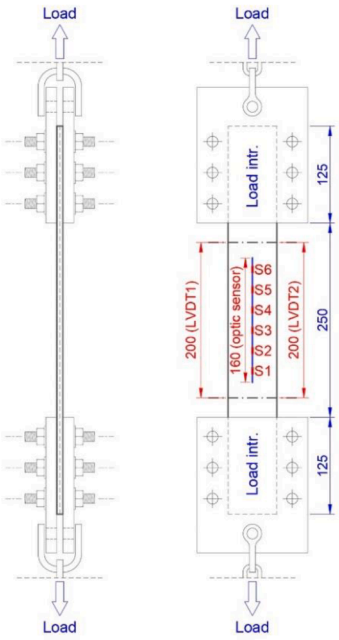

-a

-b

Fig. 3. Tensile test setup and instrumentation: schematization (-a) and positioning of the specimen in the loading machine (-b).

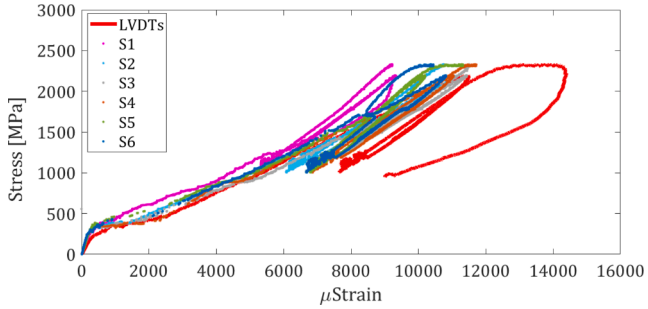

Fig. 4. Tensile stress – strain diagram obtained with the LVDTs and the fiber optic sensors.

torque wrench, so that a compression corresponding to 65% of the minimum strength of the mortar declared by the supplier (M20) was imposed to the coupon at the load introduction areas. Each of the clamping systems was connected to the test machine using a double joint as to make spherical hinges. The test was carried out in deformation-controlled mode, imposing a strain rate of $2 \times 10^{-3}/min$. During the test, two Linear Variable Displacement Transducers (LVDTs) measured the elongation of the central portion of the specimen (base length 200 mm) and the FO sensor measured the axial deformation at six points of the central yarn of the PBO mesh ("S1″-"S6″ in Fig. 3a).

The stress-strain diagram obtained from the test is reported in Fig. 4; the strain values reported in abscissa refer to the average of the LVDTs and fiber optic (FO) sensors measurements, while the stress values in ordinate refer to the nominal cross section of the textile mesh. The stress-strain diagrams show a typical trilinear shape, as expected.

Although the trend of the stress-strain diagrams of the LVDT and FO sensors is similar since it underlines the three common phases characterizing the tensile behavior of FRCM: pre-crack, cracking developing and post-crack, the diagrams of FO sensors are neither coincident among them nor with the diagram of LVDT. This feature is strictly related to the behavior of the specimen observed during the test which was characterized by a progressive formation in the matrix of six main cracks located at different sections (a more detail explanation is reported in the following, where the corresponding theoretical model is presented and validated). Indeed, while the diagram of LVDT globally accounts for the formation of cracks (the corresponding strains were deduced dividing the displacements of LVDT by their length, 200 mm, which covers a portion of the specimen where the majority of cracks occurred), the measurements provided by FO sensors are instead locally influenced by the crack formation. In particular, since the formation of each crack leads to a local redistribution of stresses between matrix and grid, the measurements provided by the FO sensors (particularly the ones close to

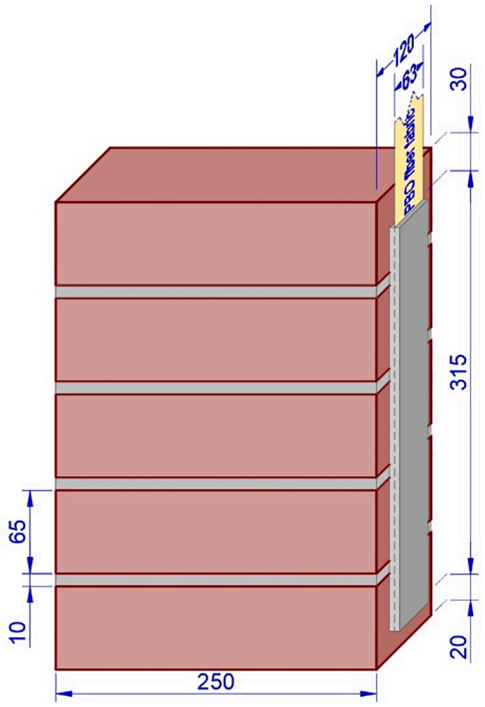

Fig. 5. Geometry of reinforced masonry pillars – SLS test. Dimensions in mm.

-a -b -c

Fig. 6. Strengthened masonry pillar manufacturing; (-a) preparation of the surface to be reinforced and formwork positioning; (-b) application of the PBO mesh equipped with the FO sensor to the first layer of mortar; (-c) application of the second layer of mortar.

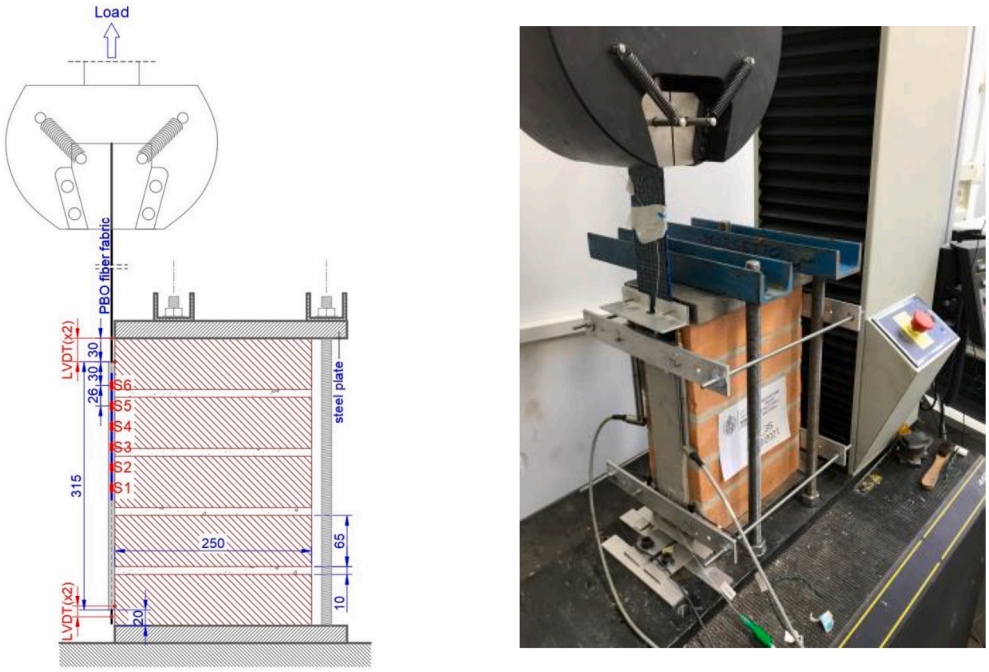

-a -b

Fig. 7. SLS test – setup and instrumentation: schematization (-a) and positioning of the specimen in the loading machine (-b).

the cracks) are able to capture this phenomenon.

2.4. Single lap shear test

The geometry of the strengthened masonry specimen subjected to a single lap shear test is schematized in Fig. 5. The masonry specimen was manufactured with five bricks ($250 \times 120 \times 65 mm^3$) and four mortar joints having thickness of 10 mm. One face of the so obtained masonry pillar was strengthened with a FRCM strengthening having dimensions $63 \times 315 \times 8 mm^3$; the thickness and the width of the strengthening are the same as considered for the coupon.

The geometric characteristics of the strengthening and the distances from the edges of the reinforced surface agree with the indications provided by [16]. The masonry specimen was manufactured and cured at room conditions for at least 28 days. Then, the surface to be reinforced was sanded and cleaned and the FRCM reinforcement was realized following a wet-lay-up procedure, analogous to the one previously described for the coupon manufacturing (see Fig. 6). Also, in this case, an FO sensor was installed to the central yarn of the PBO mesh before manufacturing the strengthening.

The test was carried out according to [16]. The specimen was constrained between two steel plates, positioned at the top and bottom, connected by four threaded bars; a slight precompression was applied to the specimen in order to avoid its rotation during the test (Fig. 7). The load was applied clamping the free edge of the PBO mesh, properly equipped with CFRP tabs (see Fig. 7). In order to avoid tensile failure of the free mesh outside the FRCM strengthening, this was also reinforced with a CFRP composite (see Fig. 7b). During the test, two couples of LVDTs measured the slip (relative displacement between the mesh and the masonry substrate) at the upper and lower ends of the reinforcements. Moreover, the FO sensor measured the strain of the mesh at the positions "S1"-"S6" indicated in Fig. 7a. The test was carried out under displacement control at a machine stroke rate of $0.2 mm/min$.

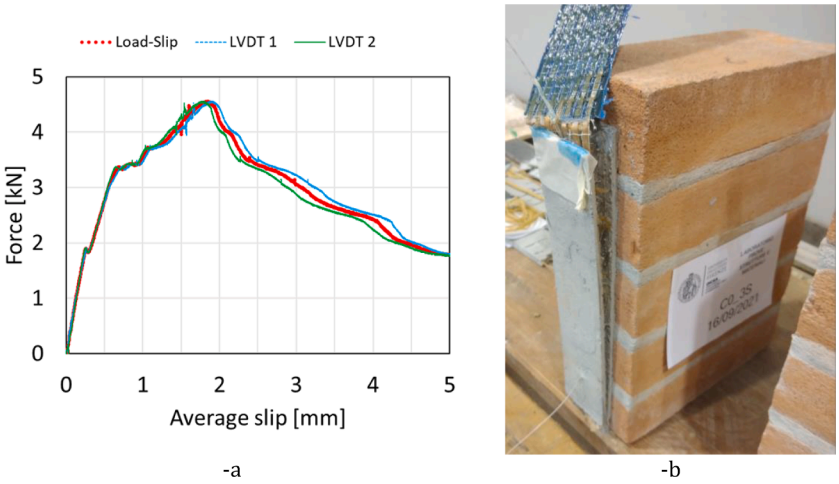

Fig. 8. SLS test: load-slip diagram (-a) and failure mode (-b).

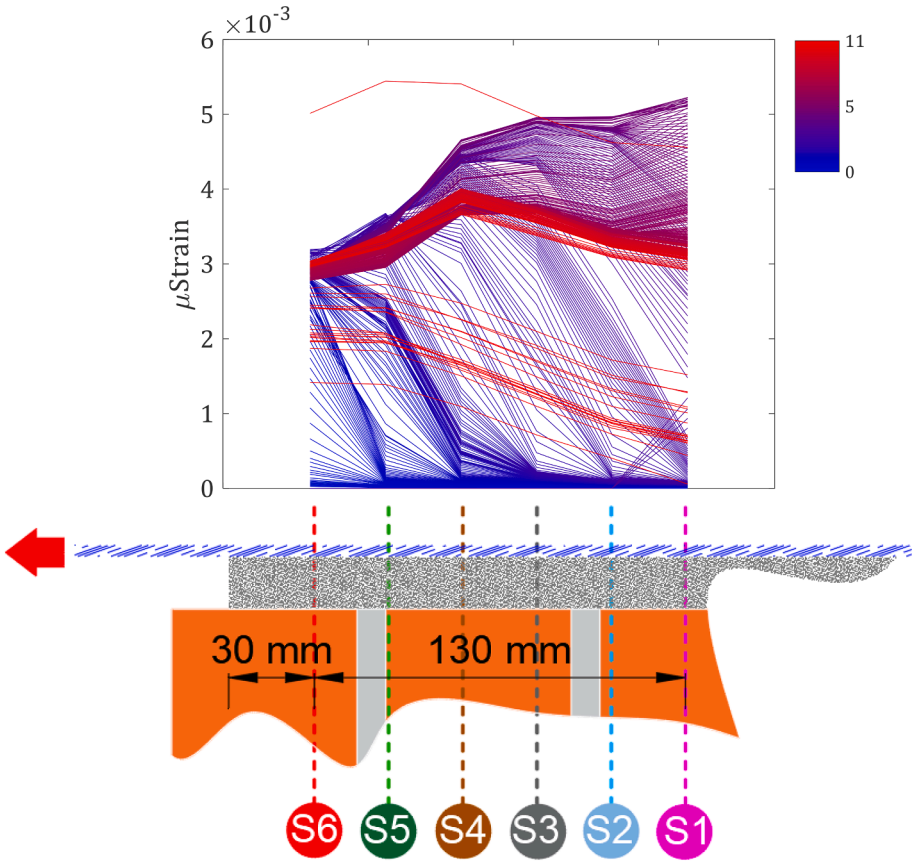

Fig. 9. Strain evolution tracked with the fiber optic sensor (colormap defined on the average displacement from vertical LVDTs – mm).

The "load"-"average top slip" equilibrium path obtained from the test is reported in Fig. 8a, while the failure mode observed at the end of the test is shown in Fig. 8b. As clearly visible from Fig. 8a, the specimen showed an initial elastic phase with gradually decreasing stiffness approaching the peak load. The decreasing stiffness was caused by the progressive cracking of the mortar matrix. No slippage was observed at this point. After reaching the peak load, the specimen started experiencing debonding phenomena involving the detachment of the textile from the mortar matrix.

3. Calibration procedure for the interfacial bond-slip law

The single lap shear test results are considered in this section to calibrate the interfacial bond-slip law obtained using FO sensors applied on the textile grid. The total bond length considered in this study was 315 mm. This value is higher than the effective bonding length estimated in [30] in 260 mm with reference to the same reinforcing system considered in the paper but bonded to concrete substrate. The portion of the reinforcement monitored during the test using FOs sensors had al length of 130 mm (see Fig. 7 and Fig. 9). Such length, although less than the effective length, was sufficient to catch all the branches of the

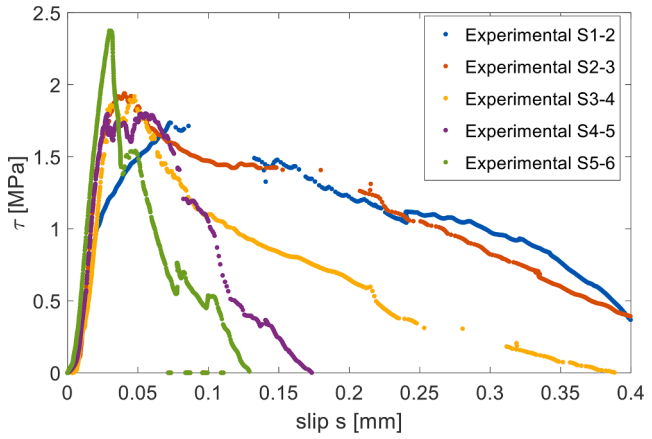

Fig. 10. Interfacial tangential bond-slip law calibrated using fiber optic sensors.

interface law. Fig. 9 depicts the strain evolutions obtained with the fiber optic sensors (Sn, n=1,2,3,4,5,6) plotted against their position along the FRCM sample. As clearly visible, the strain evolutions indicate the rising of strain levels close to the loaded end and the progressive strain shifts in the more distant parts as the anchorage length activates and the debonding process takes place. It is worth noting, FO sensors S6 and S5 recorded lower maximum strain which may be explained by edge effects or telescopic failures well documented in inorganic matrix-based strengthening materials [10,27–28]. This effect is currently under investigation with suitable sophisticated numerical and analytical models. The calibration procedure herein discussed resemble the one provided in [42] used for FRP strengthening materials neglecting the contribution coming from the support deformability. Indeed, although in current literature are available studies which specifically investigate the interaction between the grid and matrix by also taking into account the different observed behaviour at the lower and upper grid-matrix interface [43], in the present study the calibration of the parameters characterizing the grid-matrix interface law on the basis of the experimental measures is carried out by assuming the same constitutive behaviour at the both lower and upper interface and, moreover, considering an elastic behaviour for the textile grid and assuming that the deformation takes place at the interface between the textile and the lower mortar layer, average value of shear stress between two subsequent fiber optic sensors can be written as follows:

$$\tau_{1-2} = \frac{E_R{}^* A_R{}^* (\varepsilon_{i+1} - \varepsilon_i)}{b_R{}^* (x_{i+1} - x_i)} \tag{2}$$

Where, E_R, A_R and b_R are the Elastic modulus, cross section and width of PBO bundles, respectively. In this study, the following values were considered to obtain the tangential stress distribution: E_R=240 GPa, A_R=0.405 mm^2 and b_R=4 mm. It is worth mentioning that the Elastic modulus was assumed equal to the value provided by the manufacturer, the bundle cross section was estimated from the equivalent thickness provided by the manufacturer and the bundle width was measured experimentally.

In order to define the slip distribution in the FRCM sample, the following assumptions were made: (i) perfect adhesion between PBO textile and mortar matrix at the beginning of the test at the strengthening free end; (ii) the debonding process is considered to take place at the interface between textile grid and mortar matrix only; (iii) linear variation of strains in the textile grid between two subsequent fiber optic sensors. Then, integration of strain profile, starting from the free end of the strengthening material and assuming the slip at the free end to be zero, leads to the following expression for the slip at a general abscissa ×, with $x_i \leqslant x \leqslant x_{i+1}$:

$$s_i = s_{i-1} + \frac{(\varepsilon_i + \varepsilon_{i-1})^*(x_i - x_{i-1})}{2} + \varepsilon_{i-1}{}^*(x_i - x_{i-1}) \tag{3}$$

Finally, the average slip is calculated as:

$$s_{i-j} = \frac{(s_i + s_j)}{2} \tag{4}$$

In the following section, the tangential bond-slip law obtained experimentally (Fig. 10) using the procedure described in this section, is used to calibrate the analytical interfacial bond-slip law to be used in analytical models developed by the authors.

4. Analysis of the shear and tensile experimental behaviour by means theoretical models

The experimental outcomes and derived data are here analyzed throughout theoretical models finalized to simulate the behavior of specimens subjected to shear-lap tests, where the behavior at the reinforcement-matrix interface is the governing phenomenon, and, in addition, the tensile behavior of TRM/FRCM coupon, where the damage of matrix generally governs the response.

4.1. Specimens subjected to shear-lap tests

The numerical model proposed in the present Section is aimed at reproducing the experimental results obtained previously for specimen subjected to shear-lap test. The preliminary target is to fit the global load-displacement response of the specimen experimentally tested. To this scope, all the non-linearities are lumped in a fictious interface

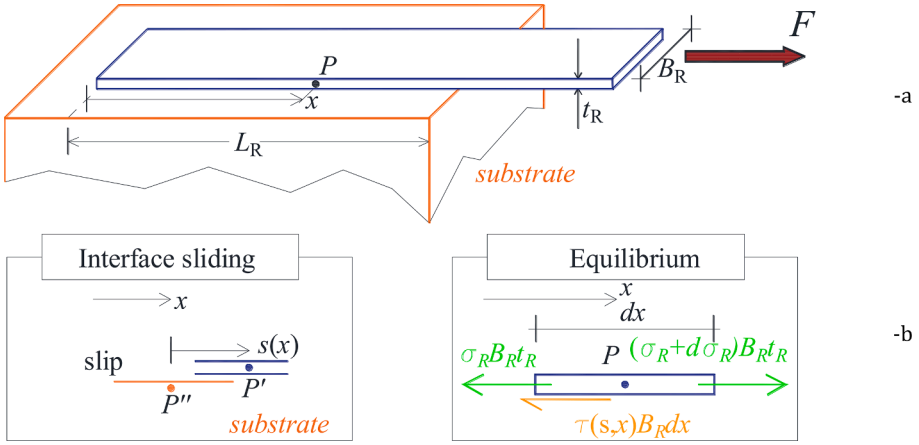

Fig. 11. Flat strengthening pack. Geometry of the strengthening system (-a) and governing equilibrium equation at the interface, with the definition of slip (-b).

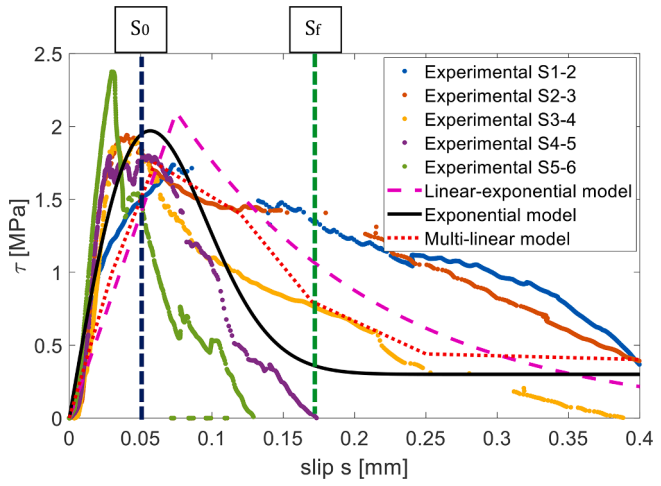

Fig. 12. Comparison among experimental interface $\tau(s)-s$ relationships and three numerical models (linear-exponential, exponential and multi-linear) adopted to fit experimental data.

located between the support and the strengthening material. Even though the authors are aware that such an assumption represents a rough simplification of the actual local behavior of a TRM/FRCM reinforcing system, because simplistically derived from approaches already in use for FRP, it can be considered reliable and globally predictive when the mode of failure is known, for instance from experimental evidence as in the case here analyzed. Having at disposal an experimental interface relationship to which to refer, a fair reproduction of the global load-displacement response in a single lap shear test is possible. Considering a TRM/FRCM or an FRP strip externally bonded to a flat surface, as in Fig. 11, it is assumed that the debonding occurs at the interface between the cementitious matrix and the reinforcing pack, without any damage inside either the support or the strengthening material [1–3]. Under such hypothesis, the obtained results turn out to be independent from the substrate properties. In addition, the strengthening material (width equal to B_R) is assumed elastic with an equivalent stiffness equal to $E_R\,t_R$ (Fig. 11-b), where E_R is the elastic modulus and t_R the equivalent thickness. Furthermore, the inelastic interface between reinforcement and substrate is supposed characterized by a Mode II fracture behavior ruled by a tangential stress $\tau(x)$-slip $s(x)$ relationship tuned on experimental data available.

As far as the numerical parameters adopted for the reinforcement in the simulations are concerned, the following numerical values are adopted, in agreement with experimental measurements: E_R=240 GPa, which corresponds to PBO dry elastic modulus; t_R=0.405/4 mm (cross section of a single bundle divided by its width, assuming the cross section rectangular for the sake of simplicity), B_R=4×7 mm, considering 7 bundles with width equal to 4 mm. The adoption for E_R of the PBO dry elastic modulus is justified by the mode of failure experimentally observed, which relies into a slippage of the grid inside the cementitious matrix.

With reference to Fig. 11b, by imposing the equilibrium along the longitudinal direction on a portion of the reinforcing pack, the following equation is obtained:

$$\frac{d\sigma_R}{dx}dx t_R B_R - \tau(s,x)B_R dx = 0 \tag{5}$$

Assuming the reinforcement elastic, then $\sigma_R = E_R\varepsilon_R(x) = E_R\frac{ds(x)}{dx}$, where $\varepsilon_R(x)$ is the axial strain of the reinforcement and $s(x)$ is the slip of the reinforcement over the support.

Substituting such relation in the previous equation, the field equation for the debonding of the reinforcement pack is obtained:

$$E_R t_R \frac{d^2 s(x)}{dx^2} = \tau(s) \tag{6}$$

Eq. (6) is coupled to initial conditions imposed on the free edge. In this way, the following Cauchy problem is obtained, which can be numerically solved by means of a standard ODE45 Runge-Kutta algorithm:

$$\begin{aligned} \frac{d^2 s(x)}{dx^2} &= \frac{\tau(s)}{E_R t_R} \\ s(0) &= s_0 \\ \left.\frac{ds(x)}{dx}\right|_{x=0} &= \frac{\sigma_R(0)}{E_R} = 0 \end{aligned} \tag{7}$$

It is interesting to point out that the imposition of a given slip s_0 at the free edge allows to transform a Boundary Value Problem BVP into a Cauchy problem (which can be tackled with explicit algorithms and therefore does not exhibit numerical convergence problems). From a mechanical point of view, the reproduction of a possible snap-back during the debonding of the interface at late stages of the loading process is very straightforward. In the present study, three different $\tau(s)-s$ relationships are assumed for the interface: (i) linear-exponential [2], (ii) exponential [344] and (iii) multi-linear.

The linear-exponential function is constituted by two phases; the first phase is linear and characterized by a stiffness equal to k. Phase 1 holds before the peak tangential stress f_b is reached. The second phase is exponential with softening, ruled by the fracture energy G_{II}. The analytical expressions of the two phases are given below:

$$\tau(s) = ks(x) \tag{8}$$

$$\tau(s) = f_b \bullet e^{\frac{-(s-s_*)\bullet f_b}{G_{II}}} = \tau_0 \bullet e^{-\frac{s\bullet f_b}{G_{II}}}, \text{ with } \tau_0 = f_b \bullet e^{\frac{s_*\bullet f_b}{G_{II}}} \tag{9}$$

In Eq. (9) s_* represents the slip value at the end of the linear elastic phase and all the other symbols have been already introduced.

The second interface model is characterized by a single exponential phase that describes both the pre-peak and the softening behavior. The corresponding $\tau(s)-s$ relationship adopted is the following:

$$\tau(s) = (\tau^* - \tau_r)\frac{s}{\bar{s}_0} e^{\frac{1}{2}\left(1-\frac{s^2}{\bar{s}_0^2}\right)} + \tau_r\left(1 - e^{-\frac{1}{2}\frac{s^2}{\bar{s}_0^2}}\right) \tag{10}$$

In the previous equation $\bar{s}_0$ is a slip parameter, τ^* and τ_r two stresses with a clear physical meaning and λ a numerical coefficient ruling the shape of the softening phase. It is interesting to point out that Eq. (10) has the property that $\lim_{s\to+\infty}\tau_I = \tau_r$, so that τ_r exhibits the physical meaning of residual tangential stress, a feature that allows the utilization of Eq. (10) for curved substrates, but that appears also suitable to study TRM/FRCM when the reinforcement grid slips inside the mortar.

The third interface model adopted for the simulations is multi-linear. The corresponding $\tau(s)-s$ relationship is derived from the knowledge of the tangential stresses at n different slips. Assuming that at two consecutive slips s_i and s_{i+1} the tangential stresses are respectively equal to τ_i and τ_{i+1}, the i-th branch of the interface $(s)-s$ law is expressed analytically as follows:

$$\tau(s) = \tau_i + \frac{s(x)-s_i}{s_{i+1}-s_i}(\tau_{i+1}-\tau_i) \tag{11}$$

According to the experimental data collected in the previous Sections, the three numerical $\tau(s)-s$ laws depicted in Fig. 12 are considered and their performance in reproducing the experimental global load-displacement curve carefully evaluated.

The parameters assumed for the first and second interface models are the following: for the first model f_b =2.1 MPa, s_*=0.075 mm and G_{II}=0.3 N/mm; for the second model$\bar{s}_0$=0.035 mm, τ^*=1.9 MPa, τ_r=0.3 MPa andλ=0.42. The solution of the Cauchy problem of Eq. (7) allows to obtain the global force–displacement curves depicted in Fig. 13 and

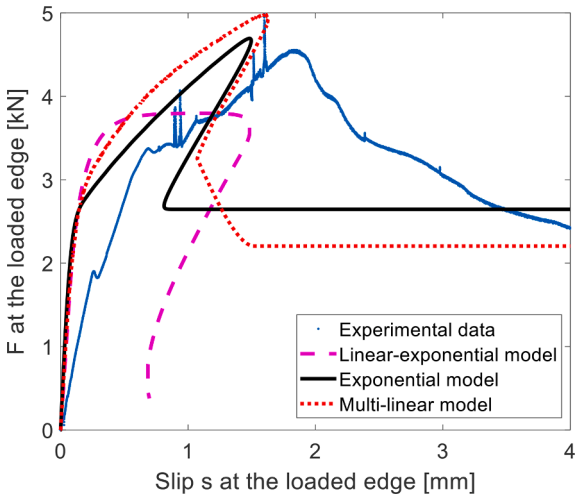

Fig. 13. Comparison between experimental global load-displacement curve and numerical predictions provided by linear-exponential, exponential and multi-linear models.

compared with the experimental data. As it is possible to notice comparing the numerical results with the experimental load-displacement curve, the fitting is quite satisfactory in all the cases, considering also the rough simplifications adopted in the models and the straightforwardness of the procedure proposed. It is worth observing that the multi-linear numerical model seems the most adequate to fit global experimental data. This is not surprising, because the interface $\tau(s) - s$ relationship adopted is capable, among the others, to closely replicate the experimental local behavior of the interface, see Fig. 12.

4.2. Specimen subjected to tensile test

A theoretical model similar to the one previously proposed for the case of shear lap tests is here employed to analyse the results deduced from the tensile test. The model is directly based on previous studies carried out by the Authors and already presented in [18,45,46].

Considering the static conditions of an infinitesimal longitudinal portion of reinforcement and a layer of matrix (Fig. 14), the translational equilibrium equations along the longitudinal direction of the reinforcement allow to write the following system of differential equations:

$$\begin{cases} d\sigma_R B_R t_R - 2\tau(s,x) B_R dx = 0 \\ d\sigma_c B_c t_c - \tau(s,x) B_R dx = 0 \end{cases} \tag{12}$$

where, additionally to symbols used in the previous model, B_c and t_c are respectively the width and thickness of the matrix layer.

Assuming a linear behaviour along the zone dx of both matrix and reinforcement:

$$\sigma_R = E_R \frac{du_R}{dx}$$

$$\sigma_c = E_c \frac{du_c}{dx} \tag{13}$$

Table 4
Parameters introduced into the theoretical model for the tensile behavior of TRM/FRCM-coupon.

Parameter	symbol [unit]	value
reinforcement Young's modulus	E_R [MPa]	240000
matrix Young's modulus	E_c [MPa]	7500
reinforcement equivalent thickness	t_R [mm]	0.045
matrix one layer thickness	t_c [mm]	4
reinforcement width	b_R [mm]	63
matrix width	b_c [mm]	63
specimen length	L [mm]	250
matrix tensile strength	f_{ct} [MPa]	2.0
bond strength	f_b [MPa]	1.9
slip at the end of the ascending branch	s_0 [mm]	0.05
slip at the end of the descending branch	s_f [mm]	0.17

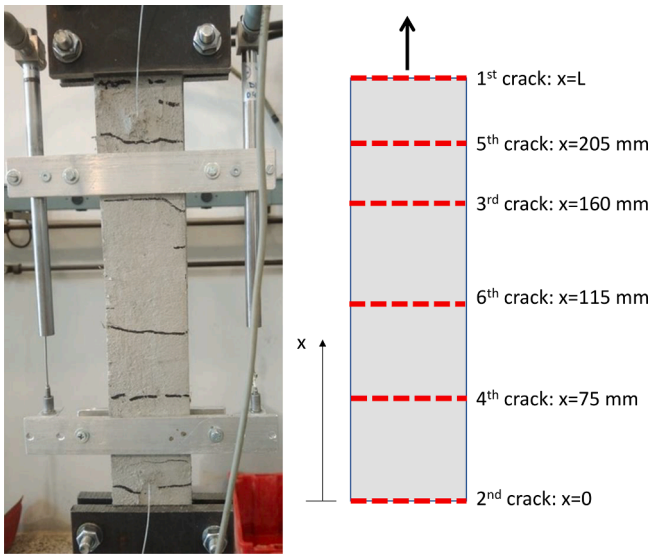

Fig. 15. Accounted crack pattern deduced from both experimental outcomes (left picture) and theoretical model (right picture).

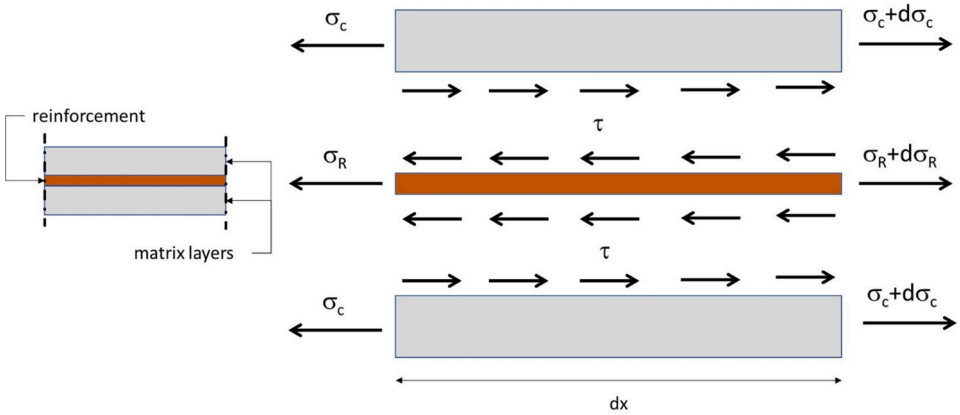

Fig. 14. Schemes accounted for deriving the equation at the basis of the theoretical model.

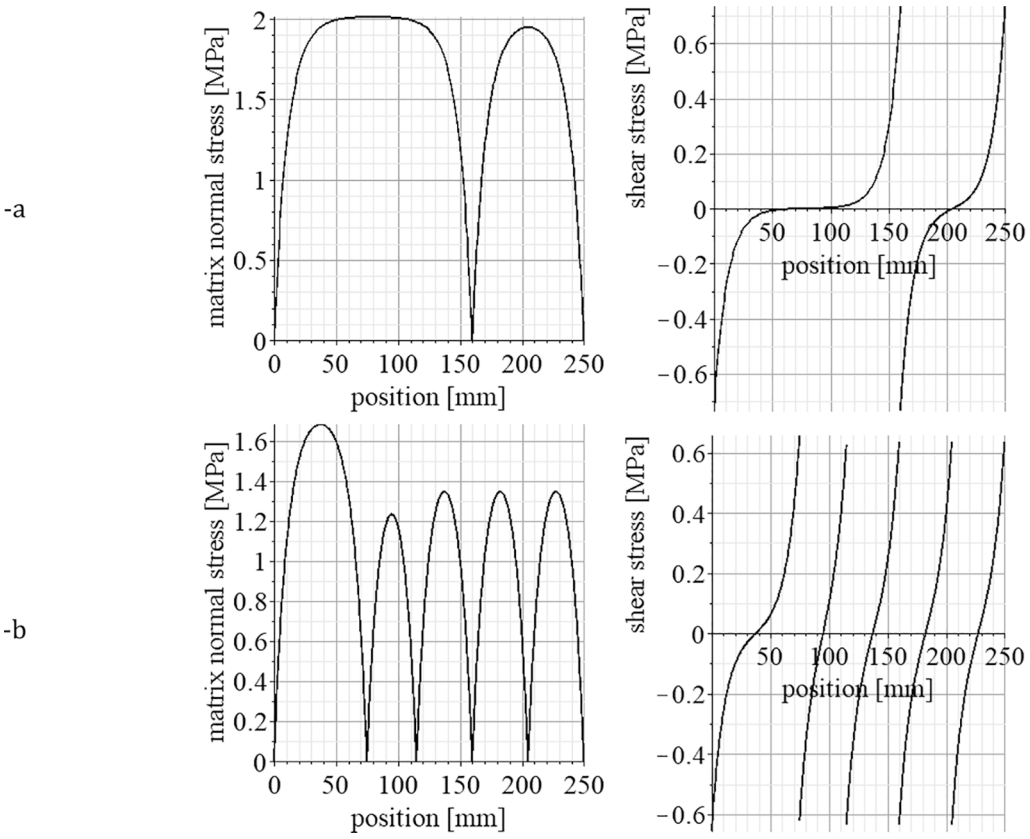

Fig. 16. Results deduced from the theoretical model at the following steps: attainment of matrix tensile strength after the formation of the third crack (-a); formation of the sixth crack (-b).

where σ_c and E_c are respectively the normal stress and the Young's modulus of matrix.

Introducing the slip s between the reinforcement and the matrix:

$$s = u_R - u_c \tag{14}$$

where u_R and u_c are respectively the axial displacement of reinforcement and matrix, it follows:

$$\begin{cases} \dfrac{d^2 s}{dx^2} - K_1 \tau(s,x) = 0 \\ \left(\dfrac{d^2 u_R}{dx^2} - \dfrac{d^2 s}{dx^2}\right) + K_2 \tau(s,x) = 0 \end{cases} \tag{15}$$

where K_1 and K_2 are two constants respectively equal to:

$$K_1 = \frac{2}{E_R t_R}$$

$$K_2 = \frac{b_R}{b_c E_c t_c} \tag{16}$$

The above system of equations can be solved as a BVP (Boundary Value Problem) adding boundary conditions, which depend on both the setup configuration (conditions imposed at the ends of reinforcement) and on the pattern charactering the formation of cracks along the matrix [18,45,46].

As far as the first conditions are concerned, taking into account the configuration of the setup here employed for tensile tests, they are the following:

$$x = 0 : u_R = 0; u_c = 0$$

$$x = L : u_R = \overline{u}; u_c = \overline{u} \tag{17}$$

where $\overline{u}$ is the displacement imposed during the test at the loaded end and L is the bond length of the specimen.

On the other hand, the formation of cracks along the matrix requires to introduce additional conditions along the length, because the field equilibrium equation on the matrix holds on single portions of the coupon separately, with an increase of the number of equations governing the problem. They depend on the number of cracks and their position, and generally consist of imposing the same value of displacement and normal stress of the reinforcement and a null value of normal stress of matrix, at the two sections across the same crack [18,45,46].

Additionally, further conditions could be necessary depending on the behaviour and the assumed constitutive shear stress-slip law of the reinforcement-matrix interface, as extensively discussed in [18,45,46] where the reader is referred for further details. Indeed, since both the cracking of matrix and the de-bonding of grid from matrix are the two possible phenomena specifically accounted for in the theoretical model, the set of equations governing the problem (number of equations and parameters characterizing the equations themselves) is strictly dependent on their occurrence during the increasing of the applied displacement. In particular, while the cracking of matrix mainly leads to an increase of the number of equations depending on the number of cracks, the occurrence of de-bonding introduces modifications of the set of equations governing the problem depending on the type of constitutive law assumed for the interface [18,45,46]. For instance, considering a multilinear law for the mesh-matrix interface, the attainment of the bond strength in some sections of specimen leads to the need to introduce additional equations necessary to describe the behaviour of the portions of specimen where the interface is in the pre-peak phase and the ones where the interface is in the post-peak phase [18,45,46].

The solution of the above system allows to simulate the tensile behaviour of TRM/FRCM coupons by analysing their behaviour at the local level.

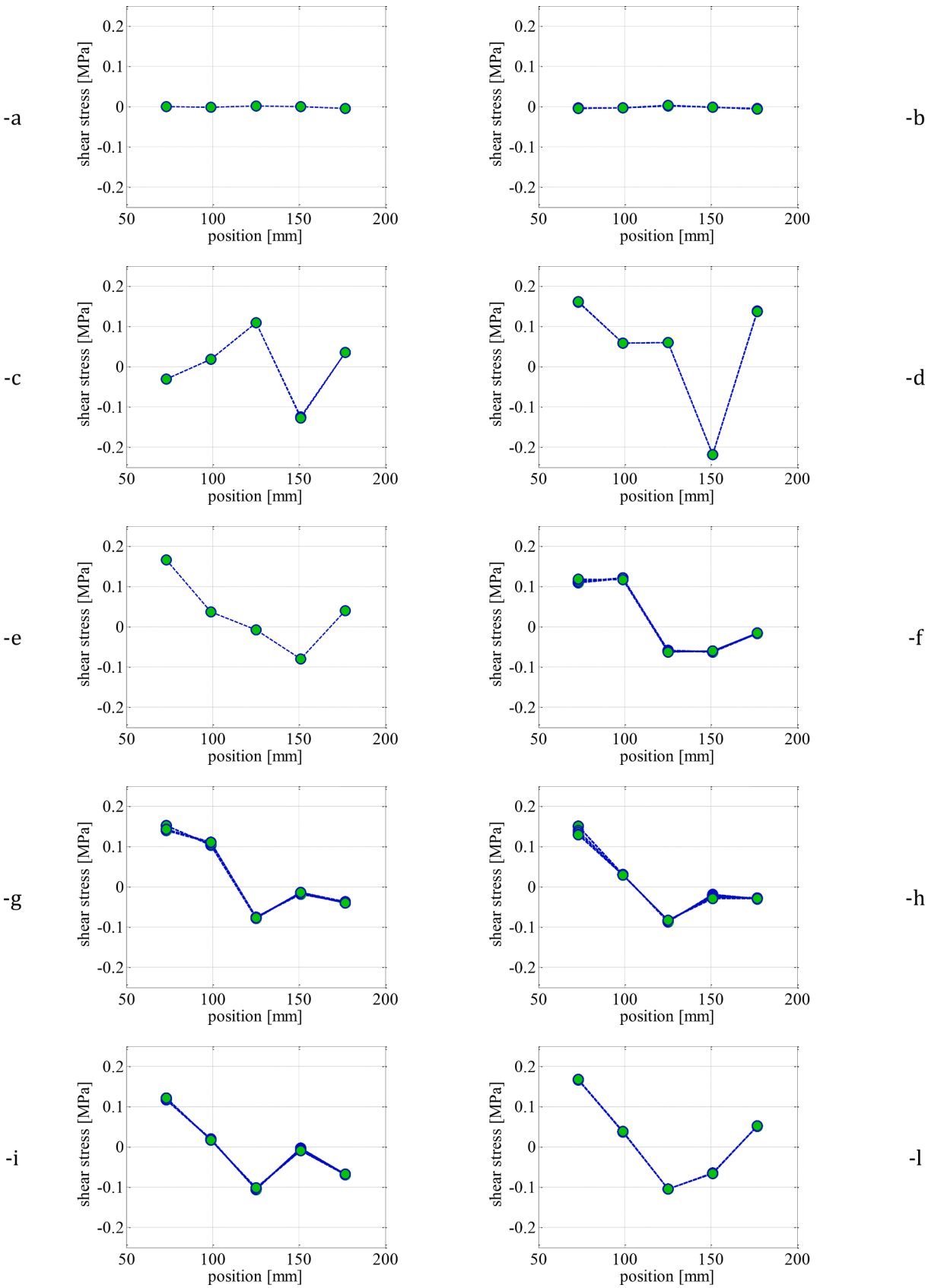

Fig. 17. Average shear stresses between two contiguous sensors derived at different load levels registered by the load cell during the tests at different level of the peak load F_{max}: 5%F_{max} (-a); 10%F_{max} (-b); 15%F_{max} (-c); 20%F_{max} (-d); 30%F_{max} (-e); 40%F_{max} (-f); 50% F_{max} (-g); 60%F_{max} (-h); 70%F_{max} (-i); 80%F_{max} (-l).

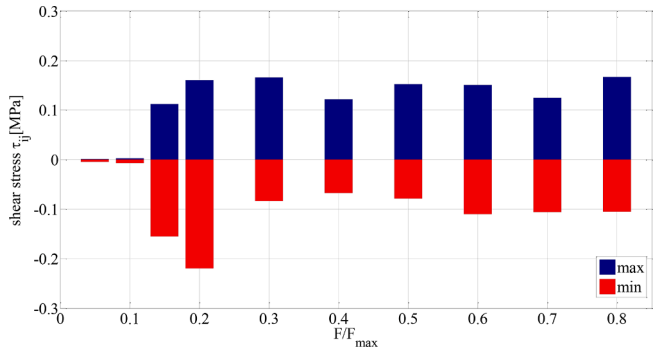

Fig. 18. Max and Min values of average shear stresses between two contiguous sensors evaluated at the different load levels.

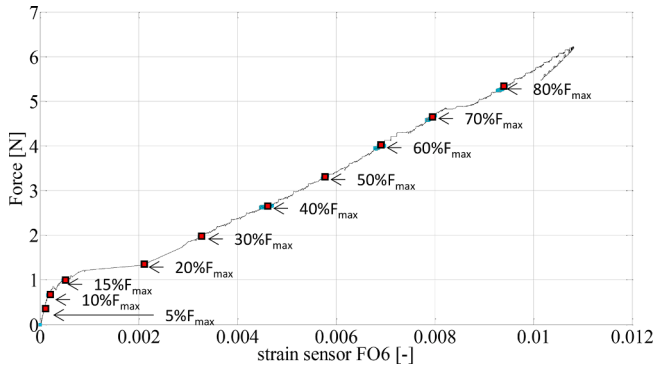

Fig. 19. Accounted load steps for deriving average shear stresses from strain measurements.

As far as the tensile test experimentally analysed in this paper is concerned, the above model is applied by considering the parameters reported in Table 4 (meaning of s0 and sf is depicted in Fig. 12) and assuming a crack pattern composed of six macro-cracks obtained by considering both the experimental outcomes and results of the theoretical model itself (see Fig. 15). In addition, one of the shear stress-slip laws previously deduced from the shear-lap test is also adopted.

Regarding the crack pattern, the following aspects are worth mentioning:

- the first two cracks are located at the loaded ends of the specimen whilst the third one at x=160 mm: the position of such cracks has been directly deduced from experimental observations carried out during the tests and considering in the theoretical model the attainment of the tensile strength of the matrix in such positions (Fig. 16a) – the position of the subsequent three cracks is directly deduced from the theoretical model at the sections where the tensile strength of the matrix is progressively attained (Fig. 16b).

The obtained crack pattern well approximates the experimentally observed one (see Fig. 15). Therefore, this crack pattern is here selected in order to perform a comparison at the local level between the theoretical and experimental results, the latter deduced from the measurements provide by optical sensors.

In particular, considering the experimental data in terms of strains directly obtained from optic sensors, an approximate estimation of the average value of shear stress τ_{ij} between two contiguous sensors i and j at one of the two interface layers can be obtained similarly to shear-lap test (see Eq. (2)), for the case of tensile test, where an equal value of shear stresses at the two interfaces is considered:

$$\tau_{ij} = \frac{E_R t_R}{2} \frac{\varepsilon_j - \varepsilon_i}{x_j - x_i} \tag{18}$$

The obtained values are presented in Fig. 17 at different levels of applied load (from 5% of the peak load to 80% of the peak load) by reporting with circular symbols the values of ij at the sections halfway between two contiguous sensors. Significant values of shear stresses can be observed (with consequent slip between reinforcement and matrix) for load levels greater than 10%. The subsequent load steps are characterized by values of average shear stresses with opposite signs: this effect is certainly due to the formation of cracks in the matrix. In particular, for both steps at 15%Fmax and 20%Fmax shear stresses with the highest value are located next to the section where the third crack occurred (x=160 mm).

A further important observation from the average shear stresses obtained from strain measurements can be deduced by analysing their peak values (both negative and positive) at different load steps, graphically presented in Fig. 18.

Indeed, it is possible to observe that, until a load level equal to about 20%Fmax, an increase of the peak values of shear stresses is observed (the maximum occurs at a load level equal to 18%Fmax); differently, the subsequent load steps are characterized by peak values of shear stresses

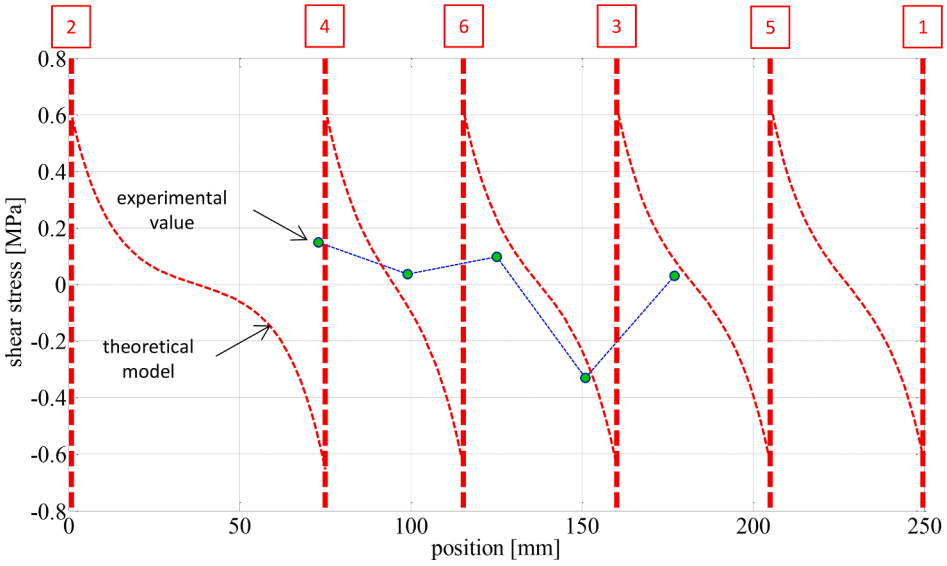

Fig. 20. Comparison between average shear stresses deduced from strain measurements (circular symbols) and shear stresses obtained from the theoretical model at the formation of six cracks (dotted lines). In the plot vertical dotted lines schematize the cracks position.

not varying in a significant manner. Such outcome is a direct effect of the crack pattern: most macro-cracks form indeed in the range 15–20% Fmax, whilst the subsequent steps are mainly influenced by the opening of the cracks. This phenomenon can be also deduced from the Force-Strain curve (see Fig. 19), where the zone characterized by the lower slope lies in this load range.

In conclusion, in order to compare the results deduced from the theoretical model and those obtained from the strain measurements, the average shear stress values deduced from Eq. (1) at the load step 18% Fmax (i.e. when all macro-cracks form in the experimentation carried out) are compared with the corresponding results deduced from the theoretical model when the formation of all six cracks occurs. The comparison presented in Fig. 20 shows a good prediction of the theoretical model particularly near the zone where the third crack arises (i.e., the one imposed in the theoretical model on the base of the experimental observation).

Finally, it is also important to observe that the values of shear stresses obtained from both experimental data and theoretical model do not reach the bond strength: this confirms in the performed tensile tests the predominance of the damage of matrix instead of the de-bonding at the reinforcement-matrix interface.

5. Conclusions

The present work provides valuable experimental results to calibrate the interfacial bond-slip law in TRM/FRCM strengthening materials and a validation of those results developed using closed form solutions already published by the authors of this work. The novelty is represented by the adoption of distributed fiber optic sensors comprising 6 sensing points installed on PBO textiles embedded into TRM/FRCM strengthening materials. The FOs sensors were used to track the local strain evolution in TRM/FRCM materials subjected to: (i) tensile tests and (ii) single laps shear tests. From the experimental and analytical investigations, the following conclusions can be drawn:

- Compared with traditional sensors (i.e., LVDTs and Strain Gauges), FOs provided valuable data on the local behaviour of TRM/FRCM coupons subjected to tensile and single laps shear tests.
- The obtained data allow for studying the tensile behaviour by analysing at the local level the influence of crack pattern on the tensile response of coupons. the results obtained from the theoretical model provide both the assessment of the laws obtained from experimental tests and, at the same time, the reliability of data furnished by the monitoring system itself.
- The local FO strain evolutions allowed to monitor the behaviour of TRM/FRCM strengthening materials tested in single lap shear tests and thus, the definition of an interfacial bond-slip law.
- The experimentally obtained bond-slip law was successfully used to calibrate different analytical models developed by the authors. The analytical force-slip curve obtained using the calibrated bond-slip law showed a very good agreement with the global experimental force-slip curve.

Finally, it is important to underline that the paper shows how the use of optical fiber sensors coupled with TRM materials can shed light on aspects that have so far been neglected in previous studies. The calibration of the interface law on the basis of the results obtained and its subsequent use in the analytical model demonstrates that such sensors can be effectively applied in these materials and, the results obtained analytically (but based on experimental data not previously available) are consistent with traditionally obtained measurements and available in the technical literature.

In conclusion, the monitoring system based on the use of optic sensor is a valuable strategy for experimentally characterizing the behaviour of TRM and FRCM strengthening systems at local level, both regarding the tensile behaviour of coupons, important for understanding the influence of the matrix damage, and the bond behaviour at the level of the matrix-strengthening interface.

CRediT authorship contribution statement

Elisa Bertolesi: Methodology, Conceptualization, Formal Analysis, Data curation, Investigation, Writing – original draft, Writing – review & editing, Visualization. **Mario Fagone:** Methodology, Conceptualization, Formal Analysis, Data curation, Investigation, Writing – original draft, Writing – review & editing, Visualization. **Tommaso Rotunno:** Methodology, Conceptualization, Formal Analysis, Data curation, Investigation, Writing – original draft, Writing – review & editing, Visualization. **Ernesto Grande:** Methodology, Conceptualization, Formal Analysis, Data curation, Investigation, Writing – original draft, Writing – review & editing, Visualization. **Gabriele Milani:** Methodology, Conceptualization, Formal Analysis, Data curation, Investigation, Writing – original draft, Writing – review & editing, Visualization.

Declaration of Competing Interest

The authors declare that they have no known competing financial interests or personal relationships that could have appeared to influence the work reported in this paper.

References

[1] J. Vaculik, P. Visintin, N.G. Burton, M.C. Griffith, R. Seracino, State-of-the-art review and future research directions for FRP-to-masonry bond research: Test methods and techniques for extraction of bond-slip behaviour, Construction and Building Materials 183 (2018) 325–345.
[2] G. Milani, E. Grande, E. Bertolesi, T. Rotunno, M. Fagone, Debonding mechanism of FRP strengthened flat surfaces: Analytical approach and closed form solution, Construction and Building Materials 302 (2021), 124144.
[3] G. Milani, M. Fagone, T. Rotunno, E. Grande, E. Bertolesi, Development of an interface numerical model for C-FRPs applied on flat and curved masonry pillars, Composite Structures 241 (2020), 112074.
[4] H. Yuan, X. Lu, D. Hui, L. Feo, Studies on FRP-concrete interface w hardening and softening bond-slip law, Composite Structures 94 (12) (2012) 3781–3792.
[5] U. De Maio, F. Greco, L. Leonetti, P.N. Blasi, A. Pranno, An investigation about debonding mechanisms in FRP-strengthened RC structural elements by using a cohesive/volumetric modeling technique, Theoretical and Applied Fracture Mechanics 117 (2022), 103199.
[6] S. Marfia, E. Sacco, J. Toti, A coupled interface-body nonlocal damage model for the analysis of FRP strengthening detachment from cohesive material, Frattura ed Integrità Strutturale 18 (2011) 23–33.
[7] R. Fedele, G. Milani, 'A numerical insight into the response of masonry reinforced by FRP strips, The case of perfect adhesion', Composite Structures 92 (10) (2010) 2345–2357.
[8] C.A. Coronado, M.M. Lopez, Numerical modeling of concrete–FRP debonding using a crack band approach, J Compos Constr ASCE 14 (2010) 11–21.
[9] F.G. Carozzi, P. Colombi, G. Fava, C. Poggi, A cohesive interface crack model for the matrix–textile debonding in FRCM composites, Composite Structures 143 (2016) 230–241.
[10] L.A.S. Kouris, T.C. Triantafillou, State-of-the-art on strengthening of masonry structures with textile reinforced mortar (TRM), Construction and Building Materials 188 (2018) 1221–1233.
[11] V. Alecci, M. De Stefano, R. Luciano, L. Rovero, G. Stipo, Experimental investigation on bond behavior of cement-matrix–based composites for strengthening of masonry structures, Journal of Composites for Construction 20 (1) (2016) 04015041.
[12] G. De Felice, S. De Santis, L. Garmendia, B. Ghiassi, P. Larrinaga, P.o.P.B. Lourenc, D.V. Oliveira, F. Paolacci, C.G. Papanicolaou, Mortar-based systems for externally bonded strengthening of masonry, Materials and structures 47 (12) (2014) 2021–2037.
[13] P.D. Askouni, C.G. Papanicolaou, Experimental investigation of bond between glass textile reinforced mortar overlays and masonry: the effect of bond length, Materials and Structures 50 (2) (2017) 164.
[14] F.G. Carozzi, A. Bellini, T. D'Antino, G. de Felice, F. Focacci, Ł. Hojdys, L. Laghi, E. Lanoye, F. Micelli, M. Panizza, et al., Experimental investigation of tensile and bond properties of carbon-FRCM composites for strengthening masonry elements, Composites Part B: Engineering 128 (2017) 100–119.
[15] S. Barducci, V. Alecci, M. De Stefano, G. Misseri, L. Rovero, G. Stipo, Experimental and analytical investigations on bond behavior of Basalt-FRCM systems, Journal of Composites for Construction 24 (1) (2020) 04019055.
[16] G. De Felice, M.A. Aiello, C. Caggegi, F. Ceroni, S. De Santis, E. Garbin, N. Gattesco, Ł. Hojdys, P. Krajewski, A. Kwiecien, et al., Recommendation of RILEM technical committee 250-CSM: Test method for textile reinforced mortar to substrate bond characterization, Materials and Structures 51 (4) (2018) 95.

[17] G. De Felice, T. D'Antino, S. De Santis, P. Meriggi, F. Roscini, Lessons learned on the tensile and bond behavior of fabric reinforced cementitious matrix (FRCM) composites, Frontiers in Built Environment 6 (2020) 5.
[18] E. Grande, M. Imbimbo, E. Sacco, Numerical investigation on the bond behavior of FRCM strengthening systems, Composites Part B: Engineering 145 (2018) 240–251.
[19] E. Grande, B. Ghiassi, M. Imbimbo, Theoretical and FE models for the study of the bond behavior of FRCM systems, Woodhead Publishing Series in Civil and Structural Engineering, Numerical Modeling of Masonry and Historical Structures From Theory to Application, 2019, pp. 685–712.
[20] E. Grande, G. Milani, Modeling of FRCM strengthening systems externally applied on curved masonry substrates, Eng Struct 233 (2021), 111895.
[21] E. Grande, G. Milani, Procedure for the numerical characterization of the local bond behavior of FRCM, Compos Struct 258 (2021).
[22] E. Grande, G. Milani, Numerical simulation of the tensile behavior of FRCM strengthening systems, Compos Part B Eng 189 (2020).
[23] E. Grande, G. Milani, Interface modeling approach for the study of the bond behavior of FRCM strengthening systems, Compos Part B Engineering 141 (2018) 221–233.
[24] E. Grande, G. Milani, M. Imbimbo, Theoretical model for the study of the tensile behavior of FRCM reinforcements, Constr Build Mater 236 (2020).
[25] E. Bertolesi, B. Torres, J.M. Adam, P. Calderon, J.J. Moragues, Effectiveness of Textile Reinforced Mortar (TRM) materials for the repair of full-scale timbrel masonry cross vaults, Engineering Structures 220 (2020), 110978.
[26] E. Bertolesi, M. Buitrago, E. Giordano, P.A. Calderon, J.J. Moragues, F. Clementi, J. M. Adam, Effectiveness of textile reinforced mortar (TRM) materials in preventing seismic-induced damage in a u-shaped masonry structure submitted to pseudo-dynamic excitations, Construction and Building Materials 248 (2020), 118532.
[27] L. Ascione, G. de Felice, S. De Santis, A qualification method for externally bonded fibre reinforced cementitious matrix (FRCM) strengthening systems, Composites Part B: Engineering 78 (2015) 497–506.
[28] S. De Santis, F.G. Carozzi, G. de Felice, C. Poggi, Test methods for Textile Reinforced Mortar systems, Composites Part B: Engineering 127 (2017) 121–132.
[29] E. Bertolesi, F.G. Carozzi, G. Milani, C. Poggi, Numerical modeling of fabric reinforce cementitious matrix composites (FRCM) in tension, Construction and Building Materials 70 (2014) 531–548.
[30] L. Sneed, T. D'Antino, C. Carloni, C. Pellegrino, A comparison of the bond behavior of PBO-FRCM composites determined by double-lap and single-lap shear tests, Cement and Concrete Composites 64 (2015) 37–48.
[31] P. Askouni, C. Papanicolaou, Comparison of Double-Lap/Double-Prism and Single-Lap/Single-Prism Shear Tests for the TRM-to-Masonry Bond Assessment, International Conference on Strain-Hardening Cement-Based Composites, RILEM Bookseries 15 (2018) 527–534.
[32] A. Dalalbashi, B. Ghiassi, D.V. Oliveira, A. Freitas, Fiber-to-mortar bond behavior in TRM composites: Effect of embedded length and fiber configuration, Composites Part B: Engineering 152 (2018) 43–57.
[33] Y. Li, J. Bielak, J. Hegger, R. Chudoba, An incremental inverse analysis procedure for identification of bond-slip laws in composites applied to textile reinforced concrete, Composites Part B: Engineering 137 (2018) 111–122.
[34] C. Du, S. Dutta, P. Kurup, T. Yu, X. Wang, A review of railway infrastructure monitoring using fiber optic sensors, Sensors and Actuators A: Physical 303 (2020), 111728.
[35] L. Fan, Y. Bao, W. Meng, G. Chen, In-situ monitoring of corrosion-induced expansion and mass loss of steel bar in steel fiber reinforced concrete using a distributed fiber optic sensor, Composites Part B: Engineering 165 (2019) 679–689.
[36] B. Schranza, M.F. Nunesa, C. Czaderski, M. Shahverdia, Fibre optic strain measurements for bond modelling of prestressed near-surface-mounted iron-based shape memory alloy bars, Construction and Building Materials 288 (2021), 123102.
[37] M. Saidi, A. Gabor, Experimental analysis of the tensile behaviour of textile reinforced cementitious matrix composites using distributed fibre optic sensing (DFOS) technology, Construction and Building Materials 230 (2020), 117027.
[38] W. Brameshuber, et al., Recommendation of RILEM TC 232-TDT: test methods and design of textile reinforced concrete: Uniaxial tensile test: test method to determine the load bearing behavior of tensile specimens made of textile reinforced concrete, Mater. Struct. Constr. 49 (2016) 4923–4927.
[39] T. Rotunno, M. Fagone, E. Bertolesi, E. Grande, G. Milani, Single lap shear tests of masonry curved pillars externally strengthened by CFRP strips, Compos. Struct. 200 (2018) 434–448.
[40] M. Fagone, G. Ranocchiai, S. Briccoli Bati, An experimental analysis about the effects of mortar joints on the efficiency of anchored CFRP-to-masonry reinforcements, Compos. Part B-Engineering 76 (2015) 133–148.
[41] European Standard, EN 998-2 Specification for mortar for masonry – Part 2: Masonry mortar, (2016).
[42] B. Ferracuti, M. Savoia, C. Mazzotti, Interface law for FRP–concrete delamination, Composite Structures 80 (4) (2007) 523–531.
[43] C. Carloni, T. D'Antino, L.H. Sneed, C. Pellegrino, Role of the Matrix Layers in the Stress-Transfer Mechanism of FRCM Composites Bonded to a Concrete Substrate, Journal of Engineering Mechanics 141 (6) (2015).
[44] G. Milani, E. Grande, Simple bisection procedure in quickly convergent explicit ODE solver to numerically analyze FRCM strengthening systems, Composites Part B: Engineering 199 (2020) #108322, https://doi.org/10.1016/j.compositesb.2020.108322.
[45] Grande E., Imbimbo M., Sacco E. (2017), 'Local bond behavior of frcm strengthening systems: Some considerations about modeling and response', Key Eng. Mater., vol. 747 KEM, 2017, p. 101–7.
[46] E. Grande, M. Imbimbo, S. Marfia, E. Sacco, Numerical simulation of the de-bonding phenomenon of FRCM strengthening systems, Frat Ed Integrita Strutt 13 (2019) 321–333.